The Astrophysical Journal, 825:115 (17pp), 2016 July 10 doi:10.3847/0004-637X/825/2/115

TESTING THE WAVELENGTH DEPENDENCE OF COSMOLOGICAL REDSHIFT DOWN TO $\Delta z \sim 10^{-6}$

Ignacio Ferreras[1,4] and Ignacio Trujillo[2,3]

[1] Mullard Space Science Laboratory, University College London, Holmbury St Mary, Dorking, Surrey RH5 6NT, UK; i.ferreras@ucl.ac.uk

[2] Instituto de Astrofísica de Canarias, E-38200 La Laguna, Tenerife, Spain

[3] Departamento de Astrofísica, Universidad de La Laguna, E-38205 La Laguna, Tenerife, Spain

Received 2015 August 1; revised 2016 May 24; accepted 2016 May 24; published 2016 July 11

ABSTRACT

At the core of the standard cosmological model lies the assumption that the redshift of distant galaxies is independent of photon wavelength. This invariance of cosmological redshift with wavelength is routinely found in all galaxy spectra with a precision of $\Delta z \sim 10^{-4}$. The combined use of approximately half a million high-quality galaxy spectra from the Sloan Digital Sky Survey (SDSS) allows us to explore this invariance down to a nominal precision in redshift of 10^{-6} (statistical). Our analysis is performed over the redshift interval $0.02 < z < 0.25$. We use the centroids of spectral lines over the 3700–6800 Å rest-frame optical window. We do not find any difference in redshift between the blue and red sides down to a precision of 10^{-6} at $z \lesssim 0.1$ and 10^{-5} at $0.1 \lesssim z \lesssim 0.25$ (i.e., at least an order of magnitude better than with single galaxy spectra). This is the first time the wavelength-independence of the $(1 + z)$ redshift law is confirmed over a wide spectral window at this precision level. This result holds independently of the stellar population of the galaxies and their kinematical properties. This result is also robust against wavelength calibration issues. The limited spectral resolution ($R \sim 2000$) of the SDSS data, combined with the asymmetric wavelength sampling of the spectral features in the observed restframe due to the $(1 + z)$ stretching of the lines, prevent our methodology from achieving a precision higher than 10^{-5}, at $z > 0.1$. Future attempts to constrain this law will require high quality galaxy spectra at higher resolution ($R \gtrsim 10{,}000$).

Key words: cosmological parameters – cosmology: observations – galaxies: distances and redshifts – techniques: spectroscopic

1. INTRODUCTION

Since the seminal work of Hubble & Humason (1931) on the recession velocities of extragalactic nebulæ, the connection between the redshift of distant sources and the evolution of the universe has been the central pillar of observational cosmology. Due to the expanding nature of our universe, light from distant sources is redshifted following a simple scaling law $\lambda_{\rm obs} = \lambda_0(1+z)$, where $\lambda_{\rm obs}$ is the observed wavelength and λ_0 is the wavelength in the rest frame of the source. Although challenged in the past as a measurement of the expansion of the universe (Arp 1987), the discovery of such a trend over millions of galaxy spectra out to $z \gtrsim 7$ (e.g., Oesch et al. 2015) has been one of the major successes of our cosmological framework.

According to the $(1 + z)$ wavelength scaling law, every spectral line from an astronomical object is redshifted by the same factor. Current individual optical galaxy spectra allow us to explore this stretching effect with an accuracy of the order of 10^{-4}. So far, no evidence has been found regarding a deviation from the theoretical prediction at this level of precision. However, with the advent of large spectroscopic galaxy surveys, such as the Sloan Digital Sky Survey (SDSS, York et al. 2000), containing millions of spectra, it is possible to explore the cosmological redshift law, statistically achieving a much higher accuracy. In fact, by combining the information from all available, high-quality galaxy spectra in SDSS, it is possible to explore any departure from the predicted, wavelength-independent, trend by a factor 100 times more accurately than with individual galaxy spectra.

The aim of this paper is to quantify any deviation from the standard cosmological redshift law in galaxy spectra when the analysis is conducted with a (statistical) precision of 1 part-per-million. Moreover, we assess whether such deviation shows any trend with redshift or wavelength. If this were the case, a variation of the $(1 + z)$ law with cosmic time could be suggestive of new (unexplored) physical, or astrophysical phenomena. A number of potential mechanisms can be found in the literature that would produce a dependence of the redshift of the galaxies as a function of the observed wavelength. For instance, Laio et al. (1997) predicted a quantum global effect of the intergalactic plasma with the photons, changing the energy of the photons without altering their trajectory. Hence, a cumulative effect along the line of sight caused by the interaction of light with the ionized material of the intergalactic medium is a potential scenario. With regards to a possible cosmological origin, one could consider changes in the fundamental laws governing null geodesics in a cosmological background that would introduce a chromatic term, breaking Lorentz invariance (introducing a wavelength-dependent speed of light Amelino-Camelia et al. 1998; Abdo et al. 2009; Arai et al. 2016). Alternatively, a change in the laws that govern the atomic emission and absorption processes (Webb et al. 2001; Quast et al. 2004; Rahmani et al. 2014; Albareti et al. 2015) could be responsible for a wavelength-dependent redshift. Finally, it is worth mentioning that well-known physical mechanisms could produce a non-cosmological redshift, such as the Wolf effect (Wolf 1987), or gravitational redshift. The latter, at the level of accuracy presented here, could be significant. For instance, the expected variation between the gravitational redshift of a photon emitted at the center of a

[4] Severo Ochoa visitor. Instituto de Astrofísica de Canarias.

massive ($10^{11} M_{\odot}$) galaxy and a photon from a region located 1 kpc away from the center should be $\Delta z \sim 5 \times 10^{-6}$.

To pursue these goals, we focus on a wide spectral range in the optical rest-frame window (3700–6800 Å), and adopt the following ansatz:

$$\lambda_{\rm obs} = \lambda_0 (1 + z)[1 + \Delta(z, \lambda_0)], \quad (1)$$

where the departure is quantified by a non-zero $\Delta(z, \lambda_0)$, for which both a redshift and wavelength dependence are considered. We make use of the excellent database provided by the SDSS (York et al. 2000), from which we select galaxy spectra with a high signal-to-noise ratio (S/N > 15), out to redshift $z \lesssim 0.25$, within which a large number of high quality spectroscopic data can be extracted from SDSS. For each spectrum it is possible to derive the observed wavelengths of several prominent absorption and emission features. Although individual SDSS spectral lines can only give redshifts with an accuracy between 10 and 30 km s^{-1} (Abazajian et al. 2003), by combining tens of thousands of high-quality spectra, it is possible to achieve a much higher precision (~0.1 km s^{-1}).

This paper presents a test of the wavelength dependence of cosmological redshift, at the highest accuracy to date, with a statistical uncertainty of $\Delta z \sim 10^{-6}$. In Section 2 we describe the spectroscopic data set. Section 3 presents the methodology adopted to derive redshifts with a number of carefully selected features. The analysis can be subject to various systematic effects from the instrumentation, the data reduction process, or the source selection. We explore the effect of stellar populations on the derivation of the line centroids in Section 4. Additional systematic effects are discussed in the Appendix. Finally, Section 5 briefly summarizes the results.

2. SAMPLE SELECTION

Our analysis is based on the SDSS spectroscopic sample. We select from Data Release 10 all individual galaxy spectra (Ahn et al. 2014) with a median S/N in the SDSS *r* band above 15. The data set is comprised of 459,953 spectra. In order to minimize the effect of variations in the properties of the stellar populations on the positions of the centroids of the spectral features, we have to select a large number of targets—so that the statistical variations are evened out. Moreover, the sample has to comprise a galaxy population as homogeneous as possible across the redshift window—to reduce the intrinsic scatter of the centroid positions *per galaxy*. The stellar velocity dispersion has been found to correlate strongly with the properties of the stellar populations of galaxies (Bernardi et al. 2005). We select galaxy spectra within a fixed interval in velocity dispersion, $\sigma \in [100, 250]$ km s^{-1} (see Figure 1). This velocity cut reduces our working sample down to 329,867 galaxies. This selection ensures that we are typically dealing with the same type of stellar populations. However, in order to study possible biases related to variations of the stellar content, we explore in Section 4 the effect of the properties of the stellar populations in more detail, with a crucial result presented in Section 4.2. Furthermore, we analyze sub-samples with respect to color, velocity dispersion, equivalent width of the lines, or S/N (see the Appendix).

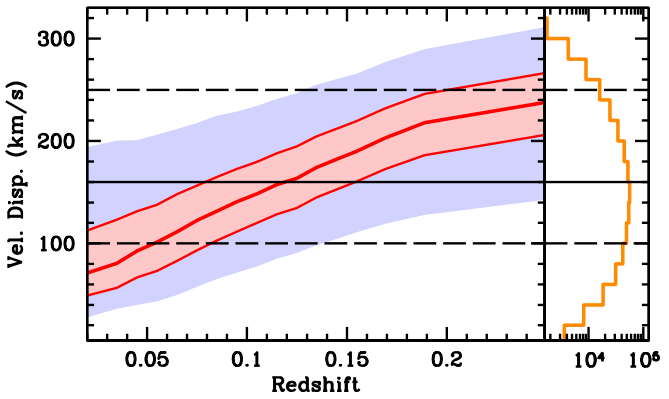

Figure 1. The sample of SDSS spectra used in this analysis is shown on the left panel as a density distribution with respect to redshift and central velocity dispersion. The thick red line traces the median of the distribution with respect to redshift, whereas the light red (light blue) shaded area delimits the region encompassing 25%–75% (5%–95%) of the sample. The orange histogram on the right is the distribution of the full sample with respect to velocity dispersion. The horizontal dashed lines mark the limit enforced for the analysis of a homogeneous galaxy sample.

3. METHODOLOGY

3.1. Spectral Line Selection

For each galaxy spectrum, we measure 60 prominent absorption or emission features, and determine their central position. To define the list of lines for the analysis, we build a reference über-spectrum by stacking 34,652 individual spectra within a 100–250 km s^{-1} range in velocity dispersion, and over a narrow redshift interval ($0.02 < z < 0.04$). The stack is visually inspected in order to select clean absorption (and some emission) lines. We avoid lines that could not be easily isolated from neighboring features, and those with an asymmetric or flat pattern. Figure 2 shows the stacked spectrum along with the full set of 60 lines initially chosen for the analysis. We select a narrow redshift bin as a reference, so that all spectral features are directly calibrated *with the same data*, avoiding biases caused by the complexity of these features (as explained in the previous section).

It is important to note that the reference lines are not produced by single atomic or molecular transitions. A galaxy spectrum is the result of an unresolved superposition of a large number of stellar spectra over a wide range of ages and chemical composition. Furthermore, the dynamical state of the galaxy introduces a strong Doppler broadening at the level of 50–400 km s^{-1}, in addition to the spectral resolution limit of the spectrograph ($R = \lambda/\delta\lambda \sim 2000$ for the SDSS spectrograph, Smee et al. 2013). Hence, each absorption line comprises a blend of many spectral features from a large number of atomic, and sometimes molecular species in the stellar atmospheres of the population (i.e., a complex mixture of spectra from stars with different mass, age, and chemical composition). This complication is inherent to the intrinsic nature of galaxies and cannot be overcome by any further improvement in instrumentation. Consequently, any study such as the one we are pursuing here, i.e., an attempt to constrain departures from the standard cosmological redshift, would be unfeasible by use of *individual* galaxy spectra.

The large data set provided by SDSS enables us to compare spectra from hundreds of thousands of galaxies, averaging out the variations in stellar properties. In addition, a careful selection of the galaxies also minimizes the variations expected

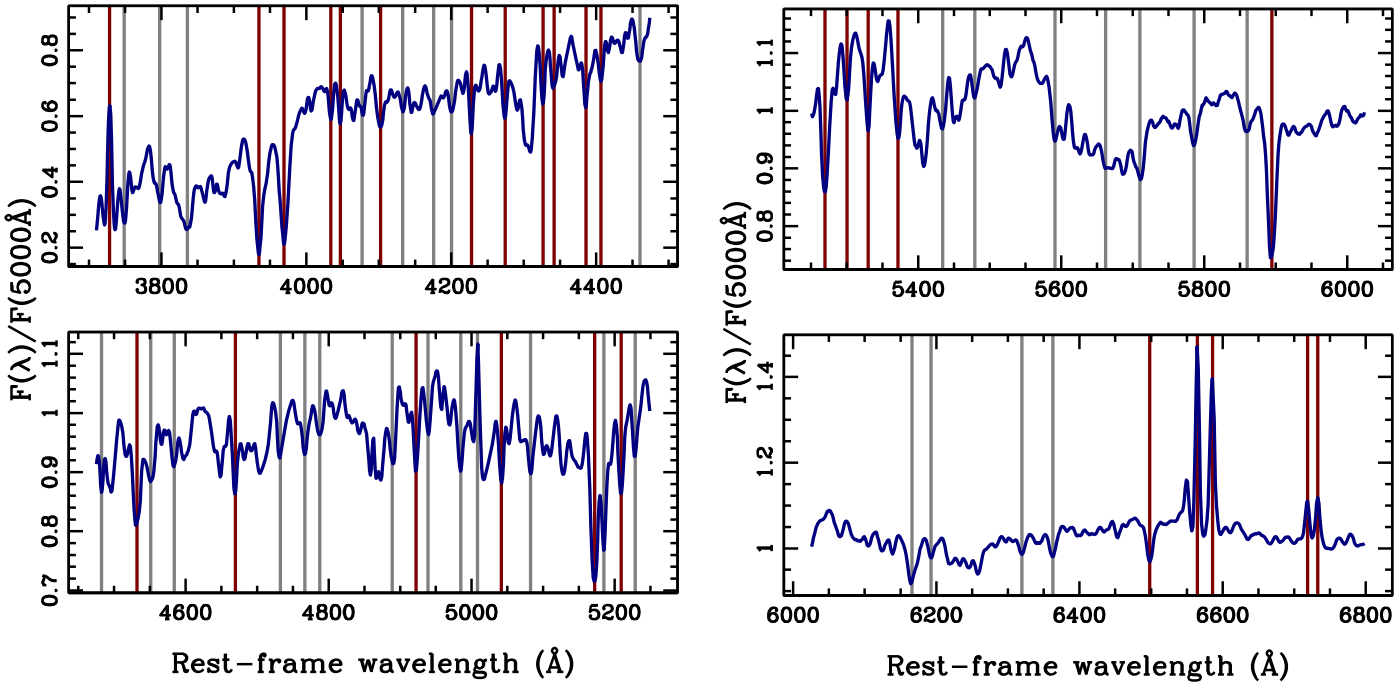

Figure 2. Selection of spectral features. A stack of 34,652 individual SDSS galaxy spectra from our sample over the redshift range $z = 0.02$–0.04 is shown along with the position of the 60 targeted lines. The 28 lines selected for the final analysis are shown in red, and the rejected lines appear in gray.

from the underlying stellar populations. In this sense, our adopted cut in velocity dispersion homogenizes the galaxy population, and helps mitigate these potential pitfalls. As the use of individual lines (atomic or molecular) from laboratory measurements is unfeasible, our methodology rests on making use of as high a number as possible of high quality galaxy spectra, and a definition of *effective central* wavelengths for a number of features, measured directly on the galaxy spectra at some fiducial redshift.[5] With these effective values we can accurately study *relative* variations with respect to redshift and wavelength.

The use of laboratory-measured lines or higher resolution stellar spectra as absolute references is also impractical because of the effect of residuals in the derivation of the index of refraction in air. The SDSS spectra are given with respect to vacuum wavelengths, using the standard conversion adopted by the International Astronomical Union (Morton 1991). Note that this conversion quotes, unchanged, an expression from an older paper (Edlen 1953). Residuals from the wavelength offset caused by a different index of refraction of air between this reference and more recent ones (Ciddor 1996) will give variations comparable to the observed shifts. We note that the prescription of Ciddor (1996) is adopted as standard by the International Association of Geodesy and is assumed to be more accurate for a wider range of conditions in atmospheric temperarure and humidity. By defining as a reference a large number of galaxy spectra *from the same sample*, within some redshift bin (in our case the redshift range from $z = 0.02$ to 0.04), we self-calibrate the positions of the lines avoiding potential biases from the air-to-vacuum wavelength conversion, and shifts of the centroids of the features caused by complex line blending effects. Additional biases due to the instrumental configuration should be minimized as well.

3.2. Determination of the Centroids of Spectral Lines

The spectroscopic data are retrieved from the DR10 DAS server of the Sloan Digital Sky Survey.[6] Only spectra are retrieved with a S/N (measured as a median value within the SDSS-r passband) above 15. The sample is further restricted in redshift between 0.02 and 0.25. A dedicated code in C reads the file, and performs line fitting on a number of prominent lines. Each individual spectrum is continuum subtracted using the BMC method of Rogers et al. (2010), with the standard choices of a 100 Å box width and a 90% level for the "boosted median." This choice has been comprehensively and independently tested to provide robust estimates of the continuum in SDSS spectra (Hawkins et al. 2014). Each line is subsequently fitted by a function

$$f(\lambda;\, \mathcal{C},\, \mathcal{A},\, \lambda_0,\, \sigma_\lambda) = \mathcal{C} + \mathcal{A} e^{-\frac{(\lambda-\lambda_0)^2}{2\sigma_\lambda^2}}. \quad (2)$$

In order to remove spurious pixels, we mask those flagged as bad pixels by the SDSS pipeline. In addition, we mask out pixels that are significantly affected by airglow. We reject fits that use fewer than six data points for each reference line. The fitting procedure is based on the Levenberg–Marquardt (Press et al. 2002) algorithm to fit the data to Equation (2), taking the measured fluxes within an interval $\Delta\lambda$ centered at the expected position of the line. The process is repeated several times for different choices of $\Delta\lambda$, and the output corresponds to the one that gives the lowest value of the χ^2 statistic, defined in the

[5] In this paper we use the galaxies in our lower redshift bin to define the central position of the spectral lines as a reference. However, the results are not affected by this choice (see the Appendix).

[6] http://skyserver.sdss.org/dr10/en/home.aspx

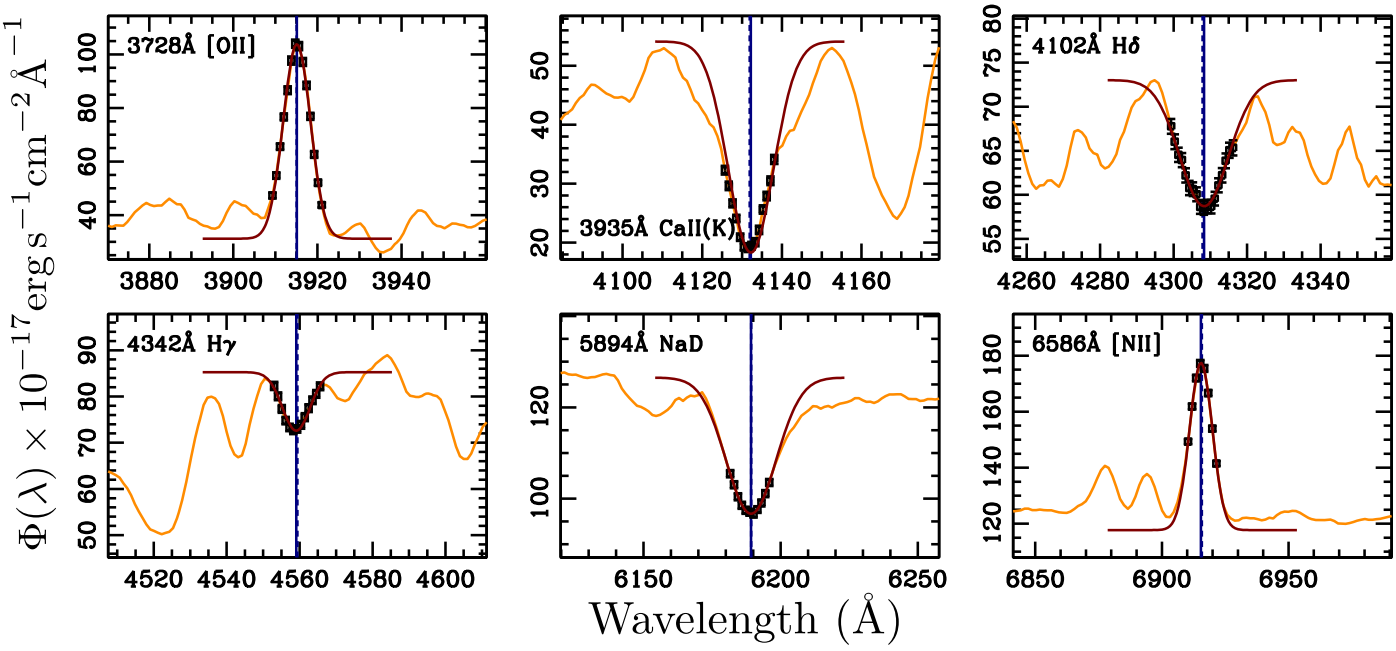

Figure 3. Examples of the line fitting procedure. The figure shows an example of the line fitting process for a typical SDSS galaxy spectrum (ID: plate-mjd-fiber ID: 545-52202-166) at redshift $z = 0.0501$ with velocity dispersion $\sigma = 186$ km s^{-1} and signal-to-noise ratio in the SDSS-r band of 35 Å^{-1}. The panels show 6 of the 28 lines used in this analysis, as labeled. The orange line is the actual spectrum; the data points used in the fit are shown with error bars. The best Gaussian fit is the red line. The vertical blue lines mark the retrieved central position of the spectral feature (solid) and the estimated position according to the redshift given by the SDSS standard pipeline (dashed).

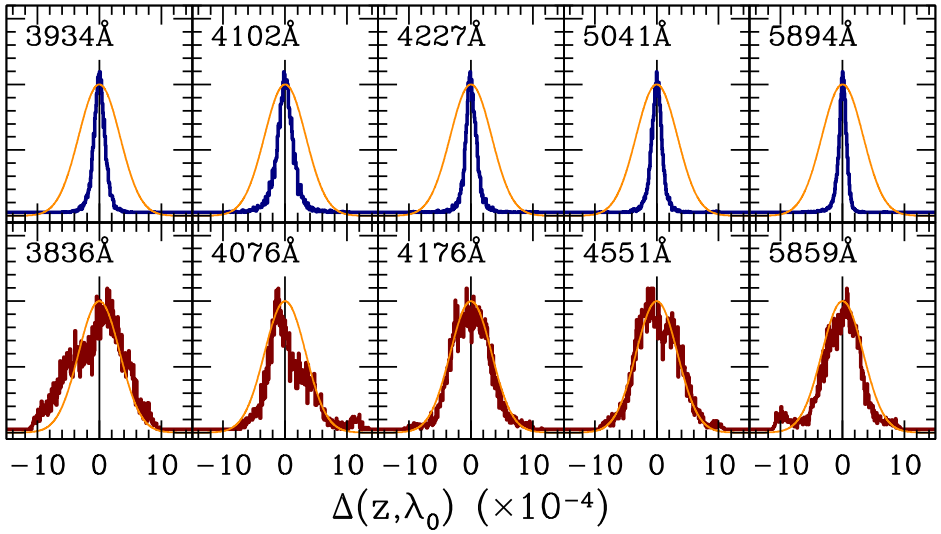

Figure 4. Behavior of $\Delta(z, \lambda_0)$ for individual lines. Typical examples are shown for lines either included (top), or rejected (bottom) in the final analysis. The histograms show the extracted value of $\Delta(z, \lambda_0)$ (as defined in Equation (1)). Each panel includes the position of the central wavelength in the rest-frame. The orange line corresponds to a Gaussian distribution with $\sigma = 100$ km s^{-1}.

standard way, namely:

$$\chi^2 \equiv \sum_{i \in \Delta\lambda} \left[\frac{\Phi(\lambda_i) - f(\lambda_i; \mathcal{C}, \mathcal{A}, \lambda_0, \sigma_\lambda)}{\sigma_i} \right]^2, \quad (3)$$

where $\Phi(\lambda_i)$ and σ_i are the observed flux and uncertainty at the sampled wavelegths, respectively. The output of the code includes the line position (λ_0), amplitude ($\mathcal{A}$) and line width (σ_λ). It also gives out the S/N of the measurement, the equivalent width, and the χ^2 of the fit. Figure 3 shows a typical example of line fitting for a few of the spectral features targeted in this analysis.

We note that the SDSS spectral pipeline (spec1d) provides for each spectrum a block of data comprising fits of emission lines (spZline[7]). A preliminary exploration of this data set showed that it is not good enough for the purposes of this work, as the fitting procedure constrains sets of lines to have the same redshift and the same width. Our method treats each spectral feature separately, with independently derived central wavelengths and line widths, and considers both emission and absorption features.

[7] https://www.sdss3.org/dr9/spectro/pipeline.php

Table 1
List of Accepted Spectral Features (List Restricted to the Reference Redshift bin: $z = 0.02$–0.04)

Line ID	Wavelength (Å)	n	EW (Å)	S/N	Comment
(1)	(2)	(3)	(4)	(5)	(6)
00	3728.3714	7287	−9.57 ± 47.18	31.81 ± 16.64	[O II]
04	3934.7674	21265	3.26 ± 1.18	28.36 ± 15.39	Ca II (K)
05	3969.3108	21035	3.48 ± 1.61	32.48 ± 17.55	Ca II (H)+Hϵ
06	4033.7667	12439	0.69 ± 0.45	59.84 ± 26.79	Fe I
07	4046.7865	11113	0.66 ± 0.47	56.95 ± 25.28	Fe I
09	4102.2947	14503	1.16 ± 0.50	61.43 ± 27.16	Hδ
13	4227.7748	12615	1.00 ± 0.48	62.85 ± 27.43	Ca I
14	4274.2991	15636	0.95 ± 0.40	65.60 ± 27.68	Fe I
15	4326.5288	13817	1.07 ± 0.42	73.18 ± 31.19	Fe I/CH
16	4341.7585	12545	1.16 ± 0.45	76.12 ± 31.21	Hγ
17	4385.9679	13459	0.83 ± 0.35	74.26 ± 33.10	Fe4383
18	4406.4512	17680	0.70 ± 0.33	79.89 ± 32.32	Fe I
21	4532.1095	17730	0.89 ± 0.44	95.65 ± 37.36	Fe4531
24	4669.4250	18104	0.60 ± 0.24	89.18 ± 33.42	$C_2$4668/Fe II/Sc II
29	4922.0688	19491	0.65 ± 0.22	96.43 ± 35.69	Fe II
33	5041.5147	19601	0.54 ± 0.21	100.88 ± 37.71	Fe I/Si II
35	5171.8832	22770	1.18 ± 0.41	91.01 ± 33.21	Mgb/Mg I
37	5209.2082	20042	0.69 ± 0.23	102.18 ± 38.80	Cr I
39	5269.5436	22210	1.00 ± 0.47	104.62 ± 39.48	Fe5270
40	5300.1071	20124	0.54 ± 0.23	109.68 ± 39.50	Cr I
41	5329.6268	21427	0.63 ± 0.23	105.84 ± 39.01	Fe5335
42	5371.5712	18110	0.48 ± 0.23	114.78 ± 41.59	Fe I
50	5894.4307	20871	1.13 ± 0.61	127.02 ± 49.20	NaD
55	6498.2663	21521	0.52 ± 0.20	145.62 ± 44.21	Ba II/Ti I/Fe I/Ca I
56	6564.7901	18729	−4.93 ± 6.77	154.33 ± 34.90	Hα
57	6585.7938	20563	−2.99 ± 3.10	151.57 ± 39.02	[N II]
58	6718.6739	18619	−1.67 ± 2.16	141.27 ± 39.37	[S II]
59	6732.8674	18175	−1.43 ± 1.60	140.97 ± 40.01	[S II]

Note. Column 1 gives the identification number of the line; column 2 is the central wavelength position after re-defining the position using the $z = 0.02$–0.04 sample as reference; column 3 is the number of galaxy spectra used to redefine the position of the central wavelength; columns 4 and 5 give the average and rms scatter of the measured equivalent width and signal-to-noise ratio, respectively. Column 6 identifies the spectral feature either by a single atomic transition, or by a well-defined spectral index commonly used in stellar population spectroscopy (Trager et al. 1998).

We begin by running the code on all spectra within the reference redshift bin ($z = 0.02$–0.04), which is comprised of 34 652 galaxies. The distribution of values of $\Delta(z, \lambda_0)$ for each line in this redshift bin is studied. For each galaxy, z is taken as the median value of the redshift from all the useful lines. Figure 4 shows the distribution of $\Delta(z, \lambda_0)$ for a few lines, showing the typical behavior of the whole set. The distributions can be split into two classes. The top panels of the figure (blue) show the histograms for lines with very small dispersion, whereas the bottom panels (red) show lines with a much noisier behavior. For reference, the orange line corresponds to a Gaussian distribution with $\sigma = 100\,\mathrm{km\,s^{-1}}$. The difference between these two sets is caused by a complex mixture of factors including the blending of neighboring lines, the typical S/N of the measurement, or the intrinsically higher variance of the features. For our purposes, we take advantage of this comparison to select a sub-sample of 28 bona fide spectral features (Table 1, and red lines in Figure 2), rejecting the rest for the analysis (Table 2). We note that the extension of the analysis to the higher redshift bins does not change the result. In other words, those lines that are well behaved in the lowest redshift interval are also well behaved in the higher redshift bins. In addition, these histograms allow us to sharpen the definition of the centroids of each spectral feature. Therefore, we re-define the central positions such that at the reference redshift $\Delta(z_{\mathrm{REF}}, \lambda_0) = 0$ for all lines. This restriction fixes the central wavelengths used as reference when measuring the departure of the $(1 + z)$ law at higher redshifts (see Table 1). This relative calibration of the line positions removes the biases described previously.

As a comparison of our measurements with the official redshift estimates from SDSS—based on a cross-correlation with a set of carefully defined templates (Aihara et al. 2011)—we find an offset z_{SDSS}–$\langle z_{\mathrm{OURS}}\rangle = (-0.981 \pm 0.013) \times 10^{-5}$, where $\langle z_{\mathrm{OURS}}\rangle$, for each galaxy, is given by the median of the redshift distribution measured by all targeted lines. Note that in contrast to the official SDSS redshift, our methodology allows us to probe the redshift as a function of wavelength. The rms scatter of the difference between SDSS and our redshift estimate is $22\,\mathrm{km\,s^{-1}}$, comparable to the quoted uncertainty of *individual* SDSS spectra (Abazajian et al. 2003). To explore any departure from the $(1 + z)$ law with redshift we divide our sample in 15 redshift bins. As a simple rule of thumb, the number of spectra within each of the 15 redshift bins is ~20,000, which implies an accuracy per bin of $0.15\,\mathrm{km\,s^{-1}}$, or $\delta z/(1 + z) \sim 5 \times 10^{-7}$.

Figure 5 shows the results of our analysis, binned in four rest-frame wavelength regions. Each bin includes a similar number of spectral features. Note that in Equation (1) we need to choose a reference redshift for each galaxy. We opted for the

Table 2
List of Rejected Spectral Features (List Restricted to the Reference Redshift bin: $z = 0.02$–0.04)

Line ID (1)	Wavelength (Å) (2)	n (3)	EW (Å) (4)	S/N (5)	Comment (6)
01	3748.4949	15272	1.96 ± 0.99	25.29 ± 12.65	Fe I
02	3797.7169	13623	1.68 ± 0.80	31.37 ± 16.51	Fe I
03	3835.8680	13614	1.57 ± 1.18	27.88 ± 14.31	Fe I
08	4076.9786	10166	0.49 ± 0.42	56.95 ± 25.82	Fe I
10	4133.0955	12271	0.52 ± 0.38	64.66 ± 27.21	Fe I
11	4175.8954	14534	0.54 ± 0.38	68.34 ± 29.50	Fe I/Fe II
12	4200.4144	15634	0.69 ± 0.37	68.64 ± 28.20	CH/Fe I
19	4460.3677	16024	0.68 ± 0.38	85.95 ± 34.84	Ca I/MnI/Fe I
20	4482.4370	9568	0.18 ± 0.34	78.74 ± 33.13	MgII
22	4551.0929	13401	0.45 ± 0.32	90.13 ± 36.16	Fe II/Ti II
23	4583.9470	15040	0.38 ± 0.24	91.97 ± 35.90	Fe II/Cr II
25	4732.5682	15838	0.44 ± 0.25	98.07 ± 38.59	Fe I
26	4766.6875	17808	0.37 ± 0.22	99.33 ± 37.71	Fe I
27	4787.3854	15123	0.41 ± 0.25	104.52 ± 39.96	Mn I
28	4888.9960	12538	0.62 ± 0.27	98.50 ± 38.50	Fe I
30	4939.1298	17205	0.50 ± 0.23	103.22 ± 37.17	Fe I
31	4984.7983	18919	0.52 ± 0.23	100.29 ± 36.70	Fe5015/Fe I/Ti I
32	5008.2542	6706	-2.19 ± 2.71	101.72 ± 34.35	[O III]
34	5082.4862	18281	0.42 ± 0.20	102.48 ± 36.99	Fe I
36	5184.9476	14656	0.58 ± 0.32	87.27 ± 31.28	Mgb/Mg I
38	5228.6874	17714	0.46 ± 0.20	107.07 ± 40.76	Fe I
43	5433.8488	15634	0.40 ± 0.21	109.89 ± 40.98	Fe I
44	5478.9656	19052	0.33 ± 0.20	112.36 ± 42.43	Fe I
45	5591.1070	5586	0.34 ± 0.17	112.41 ± 41.27	Fe I/Ca I/Ni I
46	5661.9125	474	0.27 ± 0.21	115.14 ± 46.53	Fe I/Sc II
47	5710.1112	4201	0.37 ± 0.23	121.29 ± 52.21	Fe5709
48	5785.6318	18512	0.36 ± 0.21	133.79 ± 55.23	Fe5782
49	5859.8918	15794	0.23 ± 0.19	137.94 ± 54.83	Ca I
51	6166.0155	17983	0.37 ± 0.22	141.05 ± 44.56	Ca I
52	6192.7507	18713	0.23 ± 0.15	141.46 ± 43.24	Ca I
53	6319.4290	18845	0.26 ± 0.16	140.20 ± 43.22	Fe I
54	6362.8491	19588	0.26 ± 0.23	142.72 ± 43.20	Ca I

Note. The identification of the columns follows Table 1.

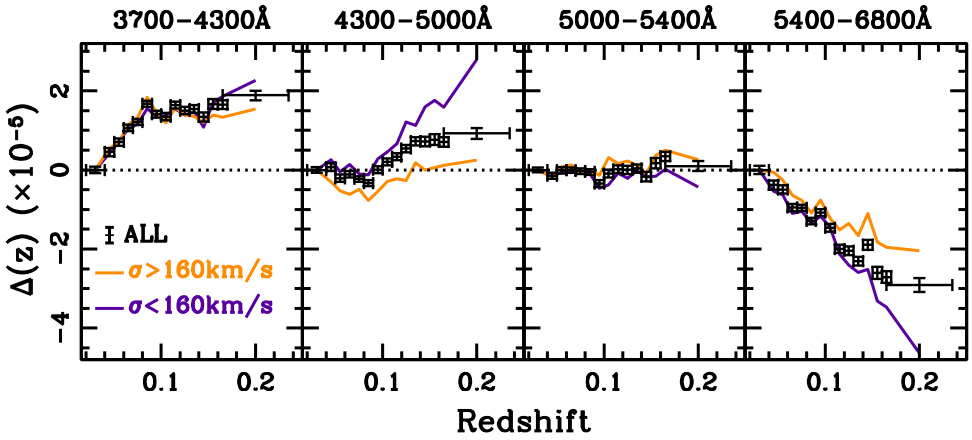

Figure 5. Deviation of the galaxy spectra with respect to a standard, wavelength-independent cosmological law, given as $\Delta(z, \lambda_0)$ (see Equation (1); the standard case corresponds to $\Delta(z, \lambda_0) = 0$). All the information from the spectral features is binned into four wavelength regions, as labeled, chosen to keep a similar number of spectral lines per wavelength bin. The data are binned in 15 steps between redshift $z = 0.02$ and $z = 0.25$. The error bars mark the mean and its uncertainty. The orange and purple lines correspond to subsamples split with respect to velocity dispersion, as labeled.

median redshift derived from all the spectral lines. The result does not change significantly if the average is used instead. The error bars represent the 68% confidence level. In order to test whether the underlying stellar populations are introducing a systematic in this result—given that the spectral features themselves are blends of many lines that can affect the centroid of the feature—we also show as orange and purple lines the results for sub-samples split according to stellar velocity

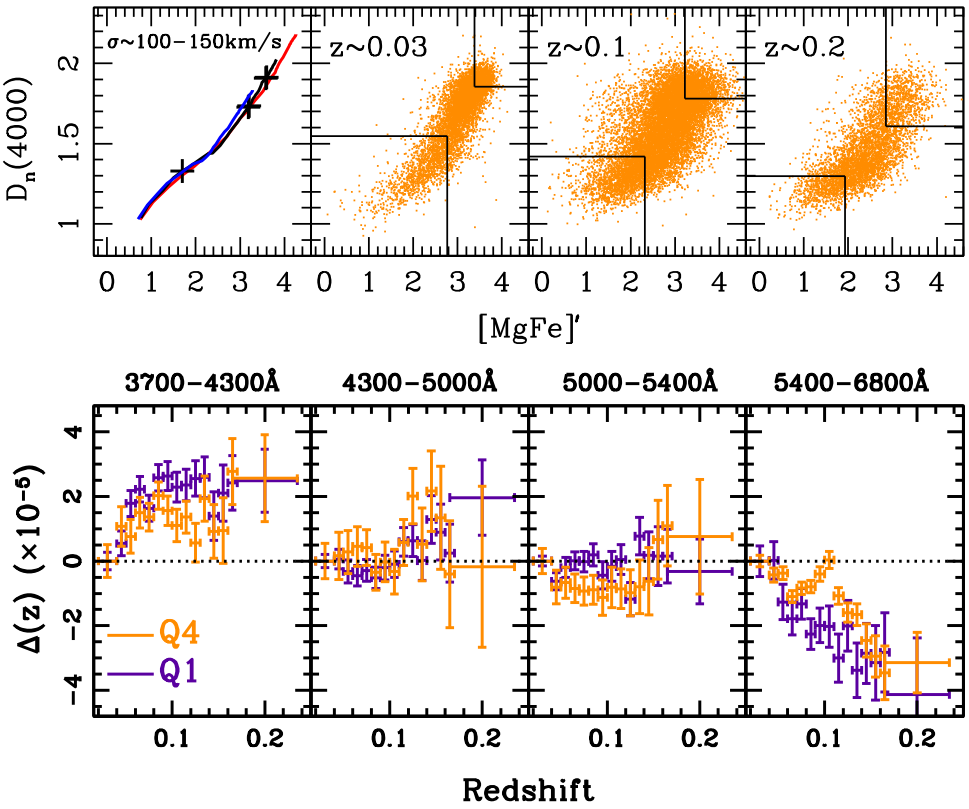

Figure 6. Top: selection of subsamples based on the age and metallicity of the underlying stellar populations (restricted to a velocity dispersion between 100 and 150 km s^{-1}). The horizontal axis shows a metal-sensitive index ([MgFe]′), and the vertical axis corresponds to the age-sensitive 4000 Å break (see the text for details). The leftmost panel shows the result for a set of simple stellar populations with metallicities [Z/H] = −0.2 (blue), 0.0 (black) and +0.2 (red), over an age range from 0.1 Gyr (bottom-left) to 13 Gyr (top-right). For reference. crosses mark the positions at 1, 5, and 10 Gyr for the model with solar metallicity. The three panels on the right show the characteristic distribution of index values for three redshift bins from our sample. The boxes mark the lowest and highest quartiles of the distribution. Bottom: results of the trend of $\Delta(z)$ with redshift restricted within each redshift bin to the lowest quartile (Q1: young and metal-poor populations, purple), and the highest quartile (Q4: old and metal-rich populations, orange).

dispersion, an observable that strongly correlates with the properties of the stellar populations (Bernardi et al. 2005). Only a mild difference is found, suggesting that the local properties of the galaxies cannot explain the observed departure of the $(1 + z)$ law. In the Appendix, we show an extensive set of tests on sub-samples split according to properties that could introduce a systematic effect, such as the S/N of the measurement, the equivalent width of the spectral feature, the observed color of the galaxy, or the effect of telluric absorption. We robustly obtain similar trends in all these tests.

4. ANALYSIS

4.1. Testing the Effect of the Age and Metallicity of the Stellar Population on the Observed Signal

Figure 5 shows a small but significant difference with respect to velocity dispersion, where the galaxy spectra at low velocity dispersion features the largest deviation from the standard cosmological $(1 + z)$ law (i.e., the highest $|\Delta(z)|$). Although this could be caused by the lower resolution produced with a higher stellar velocity dispersion, one could question whether variations in the properties of the underlying stellar populations are driving the trend reported here. Complex line blending effects affect the centroids of the lines, and a systematic difference in the stellar population composition with redshift could introduce a signal. To test this potential bias, we select subsamples of galaxy spectra based on age- and metallicity-sensitive indicators.

We choose the Dn(4000) index of Balogh et al. (1999) to trace the age-sensitive 4000 Å break, and the [MgFe]′ index defined by Thomas et al. (2003) as a metallicity-sensitive indicator. We use the index measurements of SDSS spectra from Brinchmann et al. (2004), available from the SDSS data server. The high S/N constraint imposed by our selection criteria results in accurate index measurements on individual galaxy spectra. The top panels of Figure 6 shows the index-index plot of the data in three redshift bins. Since spectral indices are sensitive to velocity dispersion, we only use galaxy spectra within the $\sigma \in [100, 150]$ km s^{-1} interval. The leftmost panel shows three tracks for a set of simple stellar populations (SSPs) from the MILES-based models of Vazdekis et al. (2012), with a Kroupa (2001) IMF. The SSPs for three different metallicities: [Z/H] = −0.2 (blue), 0.0 (i.e., solar, black) and +0.2 (red). The tracks range in age from 0.1 Gyr (bottom-left) to 13 Gyr (top-right). For reference, three crosses mark the ages 1, 5, and 10 Gyr for the track with solar metallicity. In this paper, we only need to determine whether changes in the age and metallicity distribution contribute to the observed departure from the standard cosmological law. Therefore, we perform the same analysis for the trend of $\Delta(z)$ with wavelength and redshift, as described above, restricting the sample to subsets with markedly different properties of age and metallicity. The

boxes on the three right-hand panels in Figure 6 (top) represent the lowest and highest quartiles of the distribution *within each redshift bin*. These are the subsamples we will use to explore this potential bias. We stress that this subsample is restricted to velocity dispersions between 100 and 150 km s^{-1}. The bottom panels of Figure 6 show the equivalent of Figure 5 for the young/metal-poor (Q1) and old/metal-rich (Q4) subsamples. Note that we recover a similar separation of the trend with redshift, as found with respect to velocity dispersion. The highest departure, $\Delta(z)$, is found for the younger component (i.e., the one with the lowest velocity dispersion). However, the dominant trend remains unchanged. To further assess a potential systematic caused by the effect of the stellar populations on the line centroids, we explore in the next subsection an independent approach based on population synthesis modeling.

4.2. Testing the Effect of the Methodology on the Observed Signal

The previous subsection, as well as the plethora of tests conducted in the Appendix, indicate that the observed trend in $\Delta(z, \lambda_0)$ cannot be interpreted as a result of stellar population variations with redshift. There remains the possibility that the trend is an artifact of the methodology. To test this hypothesis, we resort to population synthesis models. We create sets of synthetic galaxy spectra with the same sampling and spectral resolution as the SDSS data. We use the MILES-based models of Vazdekis et al. (2012) with a Kroupa (2001) IMF. Gaussian noise is added to the spectra, assuming a S/N = 30 in the SDSS-*r* band window, typical of the observed sample. Note that the aim of this exercise is not to test the effect of S/N on the result (see the Appendix), therefore, we do not need to adopt the same distribution of values of S/N. The data are redshifted according to the standard $(1 + z)$ law, and the same methodology is applied to these data to derive $\Delta(z)$. By construction, we should expect $\Delta(z) = 0$ in all redshift bins.

For simplicity, we adopt SSPs, where the metallicity is extracted from a Gaussian distribution with mean [Z/H] = 0.0 and rms = 0.2 dex. To assess the effect of different stellar populations, we consider three different cases, with a formation redshift fixed at $z_F = 0.5$ (i.e., dealing with younger populations), $z_F = 2$ (older populations), or taking a uniform random number between 0.5 and 2 for this formation redshift, corresponding to a more complex range of stellar ages. For each of these three cases, the synthetic sample comprises 10,000 mock spectra per redshift bin, i.e., $3 \times 150{,}000$ synthetic spectra in total.

The top three panels of Figure 7 show the trends of $\Delta(z)$ derived for these three star formation histories, using a sample with velocity dispersion drawn from a Gaussian distribution with mean 130 km s^{-1} and rms 60 km s^{-1}. For reference, the gray symbols correspond to the observed trend in the SDSS galaxy spectra. Although the observed result is not exactly reproduced, this figure confirms that the variation in $\Delta(z)$ is caused by the methodology used in this work. Before explaining how the methodology introduces such an artifact, note the relatively small difference between the three choices of formation epoch. Such an outcome suggests the variation of $\Delta(z)$ does not depend strongly on the specific details of the age and metallicity distribution of the stellar component—consistent with our negative findings in Section 4.1, or the subdominant effect when segregating the sample with respect to velocity dispersion or color (see the Appendix). On the other hand, that controls the width of the spectral features, plays an important role on the strength of the artificial signal.

The lowest panel of Figure 7 shows the result for the general case regarding the star formation history (i.e., a random formation redshift between 0.5 and 2), but with two different velocity dispersions: 230 ± 30 km s^{-1} (high σ, in red) and 130 ± 30 km s^{-1} (low σ, in blue). Note that the high velocity dispersion sample gives more compatible results with the observed SDSS data at high redshift (where the sample is dominated by high velocity dispersion galaxies, see Figure 1). Note that in the low redshift interval, $z \lesssim 0.1$, the synthetic data fully account for the signal. Therefore, in this case we can claim that the cosmological $(1 + z)$ law holds to 1 part per million.

The results of this test confirm that the signal is produced by our methodology. Moreover, the artifact is more significant in the sample with higher velocity dispersion, for which the spectral features are inherently wider. Why does our methodology introduce this signal? The derivation of the line centroids relies on the minimization of the χ^2 given by Equation (3). This minimization is conducted in the observed wavelength space. Therefore, the average number of data points for the fit increases with redshift. It is also important to note that the number of points describing the spectral features also depends on their width—that is affected by the velocity dispersion. The $(1 + z)$ stretching of the spectra also distorts the shape of the lines with redshift. This implies that as the redshift increases, the sampling of the lines in the observer frame will be slightly denser on the red side of the line with respect to the blue side. Hence, the red side of the lines has a higher effective weight, with a resulting bias on the position of the centroids. This effect is expected to be more pronounced when the feature is wide and located on the red side of the spectrum. Therefore we conclude that the bulk of the trend observed in SDSS spectra is explained as a change in *effective* resolution.

5. DISCUSSION

This paper presents a detailed analysis of a hypothetical departure of the cosmological $(1 + z)$ law with respect to wavelength. Using hundreds of thousands of high-quality SDSS galaxy spectra, we target a number of emission and absorption lines in the 3700–6800 Å rest-frame optical window, originally finding a departure from this law, parameterized by $\Delta(z)$ (see Equation (1)), at the level of $\sim 5 \times 10^{-5}$ over the redshift range $z \lesssim 0.25$, noting that our statistical accuracy reaches $\Delta\lambda/\lambda \sim 10^{-6}$. Various systematic effects are considered. We reach the final conclusion that the shapes of the absorption lines—adopted for the derivation of wavelength references—combined with the changing velocity dispersion of the sample with respect to redshift, produces an effective change in spectral resolution of these complex lines, creating the observed trend in $\Delta(z)$. No measurable departure from the standard $(1 + z)$ law is detected to within one part in 100,000 in the general sample, and to within one part per million in the redshift range $z \lesssim 0.1$. As a reference, if this result were associated with a variable speed of light across cosmic time, the analysis presented here would impose a change in c between blue ($\lambda \sim 4000$ Å) and red ($\lambda \sim 7000$ Å)

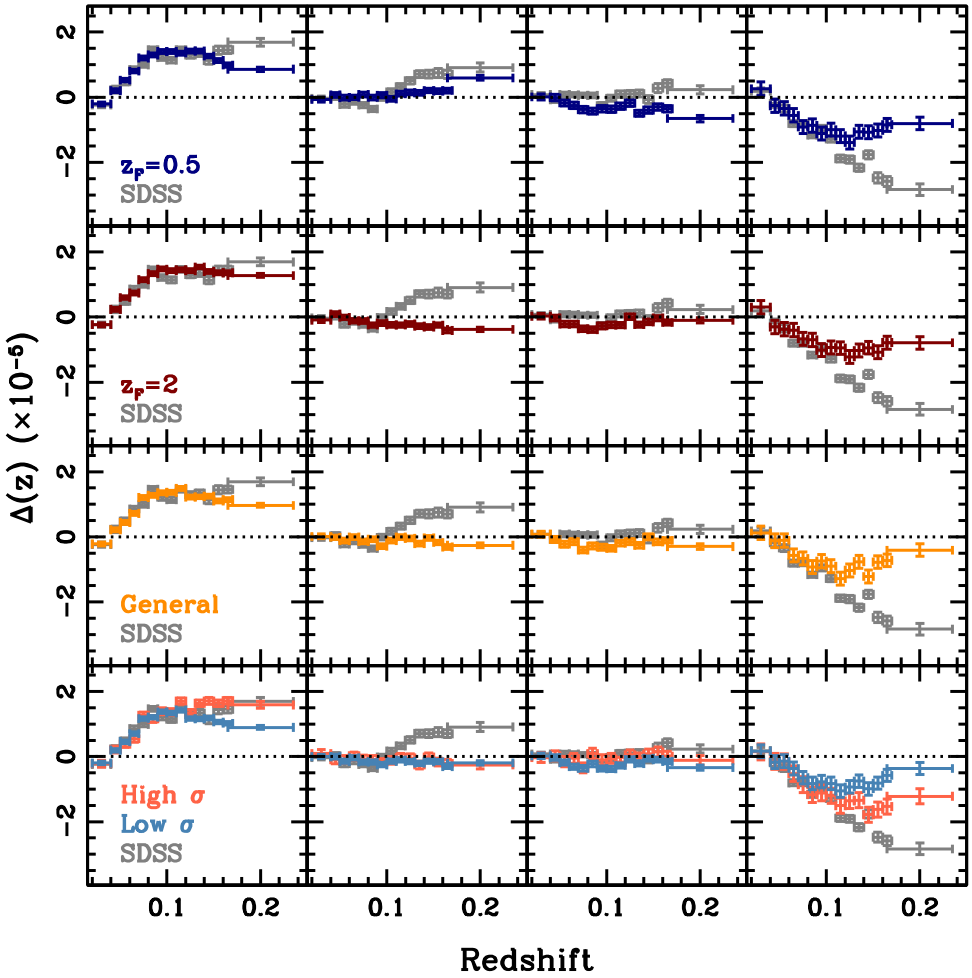

Figure 7. Trend of $\Delta(z)$ with redshift for a set of 5 × 150,000 mock galaxy spectra created from population synthesis models, with similar characteristics to the SDSS data. The colored symbols correspond to samples where the formation redshift is fixed at $z_F = 0.5$ (blue, top panels), representing overall younger populations; at $z_F = 2$ (red, middle panels), for a family of older galaxies; or for a random set of values of z_F between 0.5 and 2 (orange, bottom panels), which would better map the real populations. Note that a similar trend to the observed data (in gray) is produced by the synthetic samples, although this trend is relatively insensitive to the details of the underlying stellar populations. The top three panels are obtained from a sample with velocity dispersion 130 ± 60 km s^{-1}. The bottom panel illustrates the effect of velocity dispersion, with two subsamples: 230 ± 30 km s^{-1} (high σ, red), and 130 ± 30 km s^{-1} (low σ, blue), see the text for details.

optical photons of $\Delta c_\lambda < 300$ m s^{-1}, out to $z = 0.1$, corresponding to 1.3 Gyr in cosmic time.

The shape of the absorption lines originates from the velocity dispersion of the stars moving under the gravitational potential of the host galaxy. The Doppler shift caused by this motion blends a large number of atomic and molecular absorption lines, creating effective absorption profiles whose centroids are affected in a complex way when stretched according to redshift. The typical values of the stellar velocity dispersion in galaxies—between $\sigma \sim 100$ and 300 km s^{-1}—introduce an "effective" spectral resolution $R \sim c/\sigma \sim 2000$ that complicate the determination of wavelength references. Interestingly enough, the details of the age and metallicity distribution of the underlying stellar populations play a subdominant role, as shown in Section 4, and the Appendix, whereas a simple model of population synthesis—that combine no more than ∼1000 stellar spectra from the solar neighborhood—is capable of reproducing the observed trend in galaxy spectra.

As an aside, our data, restricted to the optical window, cannot be used to determine whether such an effect may be present in other spectral regions. Nonetheless, one can use the accurate measurement of the blackbody spectrum of the cosmic microwave background (CMB), to derive an upper limit to the expected maximum effect at longer wavelengths. The constraint provided by the CMB is not based on spectral lines, but on the (excellent) fits to a blackbody radiator. To provide a rough estimation on how the uncertainty in the CMB temperature translates into an uncertainty on the equivalent of $\Delta(z)$, let us use the position of the peak of the CMB spectrum as a wavelength reference. Using the current uncertainty on the temperature of the CMB ($T_{\rm CMB} = 2.72548 \pm 0.00057$ K, Fixsen 2009), the wavelength position of the peak is measured with the following accuracy (applying Wien's law, taking the constant from NIST[8]):

$$\lambda_{\rm CMB,peak} = 1063.22 \pm 0.43\ \mu{\rm m}.$$

Therefore the current uncertainty in the CMB allows us to measure the effect with a precision $\Delta\lambda/\lambda \sim 4.04 \times 10^{-4}$. This is an order of magnitude *larger* than the limit met by our methodology in the optical window.

Within the optical regime, previous works aiming at measuring a variable fine structure constant in quasar spectra

[8] http://physics.nist.gov/cgi-bin/cuu/Value?bwien

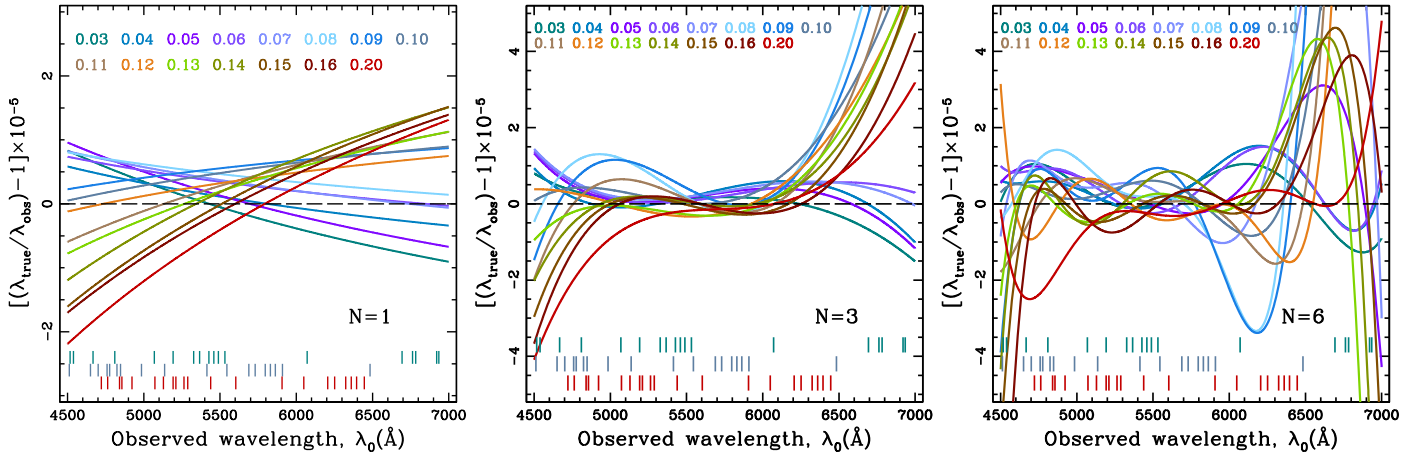

Figure 8. Testing a potential wavelength calibration residual. The most important systematic in our analysis is the effect of a residual in the wavelength calibration of the SDSS data. This figure tests such a scenario by adjusting to several polynomial transformations that recover the standard $(1 + z)$ cosmological law, with $N = 1$ (left); $N = 3$ (middle); $N = 6$ (right). Note that only the observer-frame wavelength range in common with all galaxy spectra at all redshifts is used here. The hypothesis of a calibration residual is rejected, as each redshift (colored lines with each label representing the average redshift in each bin) gives different solutions, with a manifest trend with redshift. The marks in the lower side of the panels show the position of the lines included in the analysis for three of the redshifts considered, from top to bottom: $z = 0.03$, 0.10, 0.20.

have provided to date the best constraints on wavelength departures from $(1 + z)$, with an upper limit at the level of (see, e.g., Webb et al. 2001; Quast et al. 2004; Rahmani et al. 2014; Albareti et al. 2015) $\delta\lambda_z/[(1 + z)\delta\lambda_0] \sim 10^{-5}$–$10^{-6}$ out to redshifts $z \sim 1$, where $\delta\lambda$ denotes the separation between two spectral lines, and the subscript refers to the redshift. Our results are not in contradiction with this upper limit. The studies of the variation of the fine structure constant use multiplets of a given atomic element. The targeted spectral features, such as the [O III] doublet ($\lambda\lambda$4960, 5008 Å), cover a relative narrow spectral window ($\Delta\lambda \lesssim 100$ Å). In comparison, our study covers a wavelength window at least 30 times larger.

In this context, we wonder whether analyses of the variation of the fine structure constant based on absorption lines (e.g., Quast et al. 2004) may suffer from similar type of systematic effects. In addition, the use of nebular emission lines might present equivalent systematic complications in the determination of the centroid of the line, this time caused by the gas kinematics, but such musings are beyond the scope of this paper.

Is the result shown in this paper an absolute limit to the accuracy one can achieve with galaxy spectra? Although the present data cannot provide an accuracy better than one part in 100,000 out to $z \lesssim 0.25$, we speculate that high S/N spectra at significantly higher resolution—$R \gtrsim 10{,}000$—can be used to probe in detail the effective shapes of the absorption lines, potentially allowing us to break this barrier. The denser sampling at higher resolution will decrease the statistical weight in the methodology due to differences in the number of fitting points between the blue and the red sides of the spectral features, caused by the stretching of the spectra.

The authors would like to thank Juan Betancort Rijo, Stéphane Courteau, José Alberto Rubiño Martín, Fernando Atrio Barandela, Francesco La Barbera, Martín López Corredoira, and Alexandre Vazdekis for insightful comments about this project. The referee, Dr Dan Kelson, is warmly thanked for his positive criticism, suggestions, and very hard work! I.F. acknowledges support to visit the IAC through the Severo Ochoa visitor programme. I.T. acknowledges support by the "Programa Nacional de Astronomía y Astrofísica" of the Spanish Ministry of Science and Innovation under grant AYA2013-48226-C3-1-P. Funding for SDSS-III has been provided by the Alfred P. Sloan Foundation, the Participating Institutions, the National Science Foundation, and the U.S. Department of Energy Office of Science. The SDSS-III website is http://www.sdss3.org/.

APPENDIX
POTENTIAL SYSTEMATICS

A.1. Wavelength Calibration

A.1.1. Testing the Wavelength Calibration of SDSS Spectra

In addition to the signal found in the simulated data (Section 4) one could also consider the possibility of an inaccurate wavelength calibration of the SDSS spectra. The official SDSS pipeline quotes typical errors (Abazajian et al. 2009) of order $2\,\mathrm{km\,s^{-1}}$, which translates into an uncertainty of $\delta\Delta(z;\ \lambda_0) \sim 7 \times 10^{-6}$ for individual spectra. Although this effect should be significantly lower than our measurements, especially if we consider that the whole analysis rests on the determination of approximately 6.8 million individual spectral features, we nevertheless explore below a possible systematic from a wavelength calibration trend. If the observed signal is due to a calibration wavelength problem, then we should not expect the calibration bias to depend on the redshift bin considered. Consequently, we conduct the following test: for each redshift bin we select only those lines within the common observer-frame window, between 4500 and 6800 Å. We calculate in this region how much the observed wavelengths ($\lambda_{\rm obs}$) depart from the standard $(1 + z)$ law for each redshift bin. In this test, we hypothesize that such departures are caused by an inaccurate wavelength calibration, so that the actual measurement of the wavelength should be $\lambda_{\rm true} = \lambda_0(1 + z)$. We model this wavelength calibration mismatch using a polynomial relation with $\lambda_{\rm obs}$ in each

redshift bin,

$$\lambda_{\rm TRUE} = \sum_{i=0}^{N} a_i \lambda_{\rm OBS}^i = \lambda_0 (1+z). \quad (4)$$

Figure 8 shows the result for three choices of N: a linear fit ($N = 1$; left); a cubic polynomial ($N = 3$; middle); or a sixth-order polynomial ($N = 6$; right). If a wavelength calibration were to explain the observed trend, we should find no significant variation of the solution with respect to redshift—as we use in this test the same set of spectral lines in the observer frame. The variation of the solutions with redshift confirms that the calibration solution is not compatible among redshift bins. Furthermore, this correction evolves in a smooth way with redshift, illustrating the fact that this result cannot be explained by a wavelength calibration residual.

A.1.2. Independent Wavelength Calibration Test with Sky Lines

As a further test of one of the most important instrumental systematics in this analysis, we consider a method where the derivation of the redshift offsets, $\Delta(z, \lambda_0)$, is, to lowest order, independent of the wavelength calibration solution. In this case, we make use of the sky spectra available for each SDSS galaxy spectrum. The positions of several night sky lines are used as reference points, interpolating between them to derive the positions of the spectral lines in the galaxy spectra. Therefore, this approach compares a set of wavelengths measured in galaxy spectra, $\{\lambda_i\}$—that vary according to the redshift of the galaxy—and lines in sky spectra whose central positions, $\{\mu_i\}$, are constant throughout the sample. Let us assume that a non-zero wavelength calibration residual is present, such that the observed measurements and the true measurements can be written:

$$\lambda_i^{\rm TRUE} = \lambda_i^{\rm OBS}[1 + f(\lambda_i^{\rm OBS})].$$

Given that our findings reveal a small effect with respect to the standard $(1 + z)$ law, we can safely assume that $f \ll 1$. The same relation applies to the wavelength positions of the sky lines, $\{\mu_j\}$, namely,

$$\mu_j^{\rm TRUE} = \mu_j^{\rm OBS}[1 + f(\mu_j^{\rm OBS})] \Rightarrow 1 \quad + \quad f(\mu_j^{\rm OBS}) = \left(\frac{\mu_j^{\rm TRUE}}{\mu_j^{\rm OBS}}\right)$$

Therefore, the wavelengths measured in the galaxy can be written with respect to the sky wavelengths as:

$$\lambda_i^{\rm TRUE} \simeq \lambda_i^{\rm OBS}\left(\frac{\mu_j^{\rm TRUE}}{\mu_j^{\rm OBS}}\right), \quad (5)$$

where the correction term on the right hand side is taken for the closest sky line associated to each galaxy line (i.e., $\lambda_i^{\rm OBS} \sim \mu_j^{\rm OBS}$), and we assume the wavelength positions of the sky lines in galaxies within the reference redshift bin ($z = 0.02$–0.04), are the true wavelength values for night sky lines. In a nutshell, we are using the *relative* offsets between the galaxy lines and the sky lines to derive the redshift of individual features, with the assumption that the positions of the night sky lines do not change systematically with respect to the redshift of the galaxy observed.

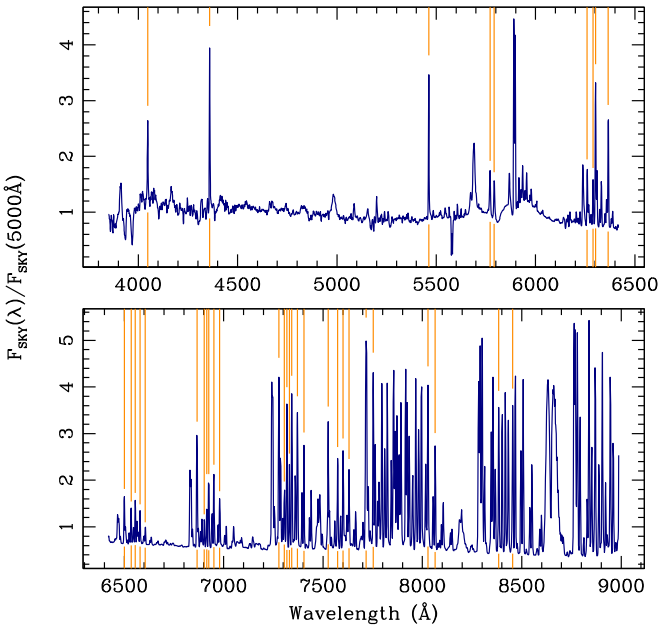

Figure 9. Stacked spectrum of the night sky obtained by median combining 34,652 SDSS spectra from the reference sample (i.e., corresponding to galaxies with $z = 0.02$–0.04). The positions of several emission lines used as reference for an independent test of the wavelength calibration are shown as orange vertical lines.

The FITS files retrieved from the SDSS server (see Section 3.2) include the night sky spectrum as an additional entry. In order to define a list of strong sky lines, we build a stack sky spectrum by combining 34,652 individual ones from the sample within the reference redshift bin. Figure 9 shows the stack along with the lines selected visually for the analysis. We selected 37 lines, making sure the S/N was high enough in individual sky spectra, and the line was not affected by the presence of neighboring lines. The top panels of Figure 10 show the equivalent of Figure 4 for several sky lines. Note these histograms are much narrower, reflecting the simpler behavior of the sky lines with respect to the blended features observed in galaxy spectra. The orange line, for reference, is also a Gaussian corresponding to a velocity dispersion of 100 km s^{-1}. The bottom panels of Figure 10 show the accuracy of the wavelength calibration. We show the $\Delta(z)$ values as a function of redshift—as in Figure 5 but estimated directly from the measurements of the sky lines. Therefore, the redshift for these measurements corresponds to that of the galaxy spectrum from which the centroids of the night sky lines are measured. A zero value of $\Delta(z, \lambda_0)$ is expected throughout. The figure confirms the lack of a systematic trend, and illustrates the level of accuracy of our data set, namely $\Delta\lambda/\lambda \sim 10^{-6}$.

Figure 11 is the equivalent of Figure 5 when the redshifts are derived using the position of the night sky lines as a reference, instead of the standard wavelength calibration solution. Note that the trend is consistent with the results using the standard wavelength calibration solution, therefore our results cannot be explained by a residual in this calibration.

A.2. Asymmetry of the spectral features

An additional systematic that one should consider is whether the shape of the features could introduce a small effect on their derived centroids. We emphasize that the lines being studied

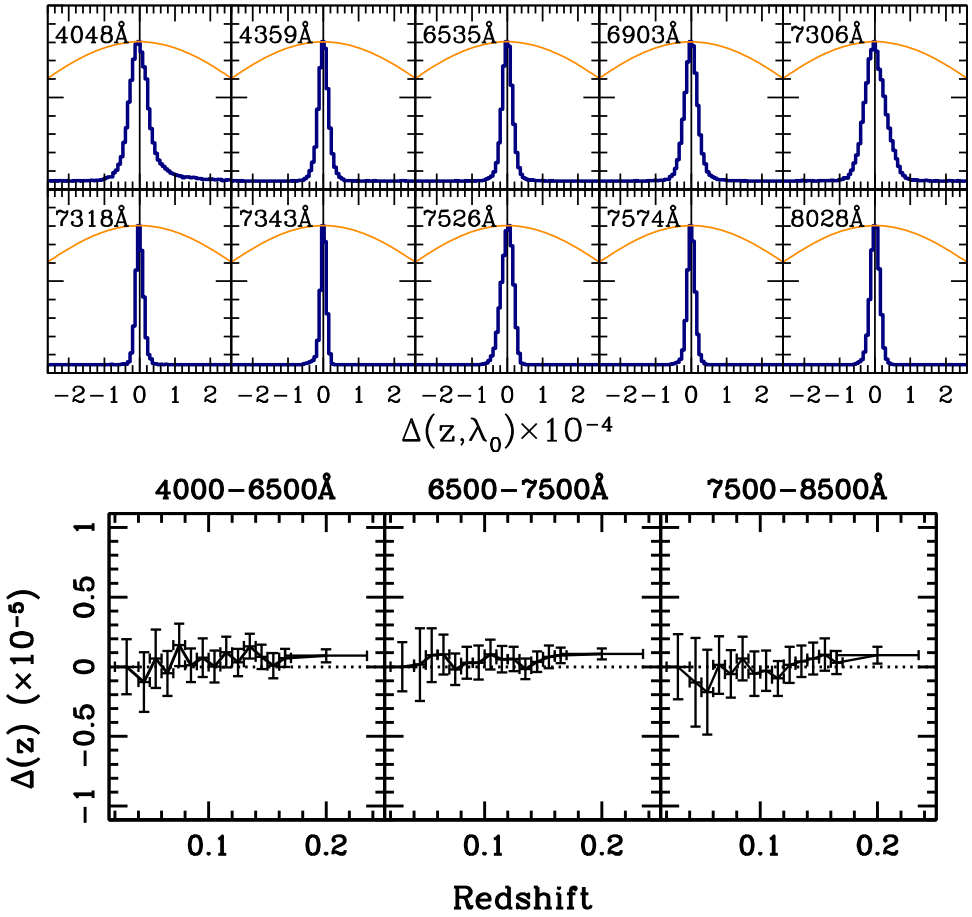

Figure 10. Top: the equivalent of Figure 4 for a set of emission lines from the night sky, used as an additional test of the wavelength calibration of the SDSS data. The orange line corresponds to a Gaussian distribution with $\sigma = 100$ km s^{-1}. Bottom: to illustrate the accuracy of our methodology, this figure presents the equivalent of $\Delta(z)$ measured directly on the night sky lines in each of the galaxy spectra (hence the association of a redshift).

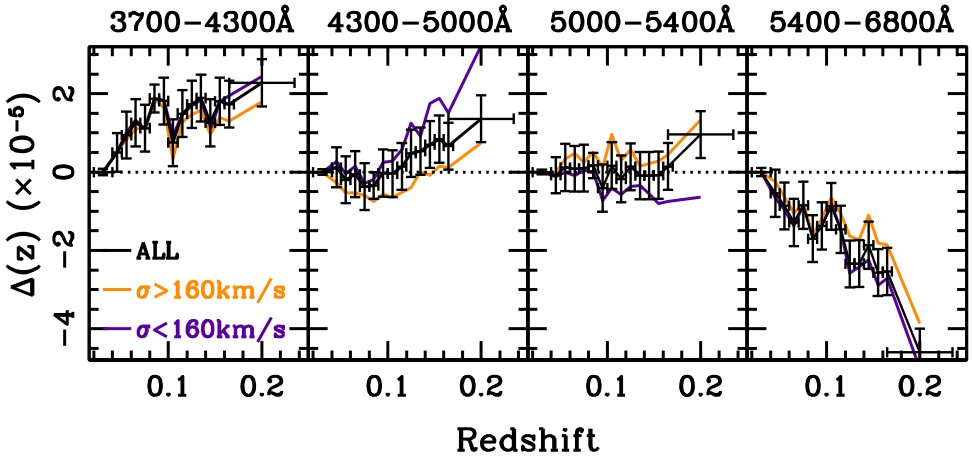

Figure 11. The equivalent of Figure 5, using the positions of night sky lines as reference, instead of the standard wavelength calibration solution. Note that the vertical axis covers the same interval in $\Delta(z)$ as in Figure 5.

here are complex superpositions of individual absorption lines blended both by the stellar velocity dispersion of the galaxy and by the resolution of the spectrograph. Note that for this effect to produce a signal in our analysis, we would need a systematic trend with respect to wavelength, as we are averaging out over several lines, comprising thousands of spectra. Nevertheless, we test here this potential systematic. Any departure from the Gaussian fit that we apply in our analysis will produce an offset of the central position if the actual line is asymmetric. Profiles such as a Lorentzian, or a Voigt profile will yield the same central position, albeit with a different line width. Therefore, we test a possible asymmetry (skewness) of the lines by comparing the residuals of the fits separately on the blue and the red side of each line. We define

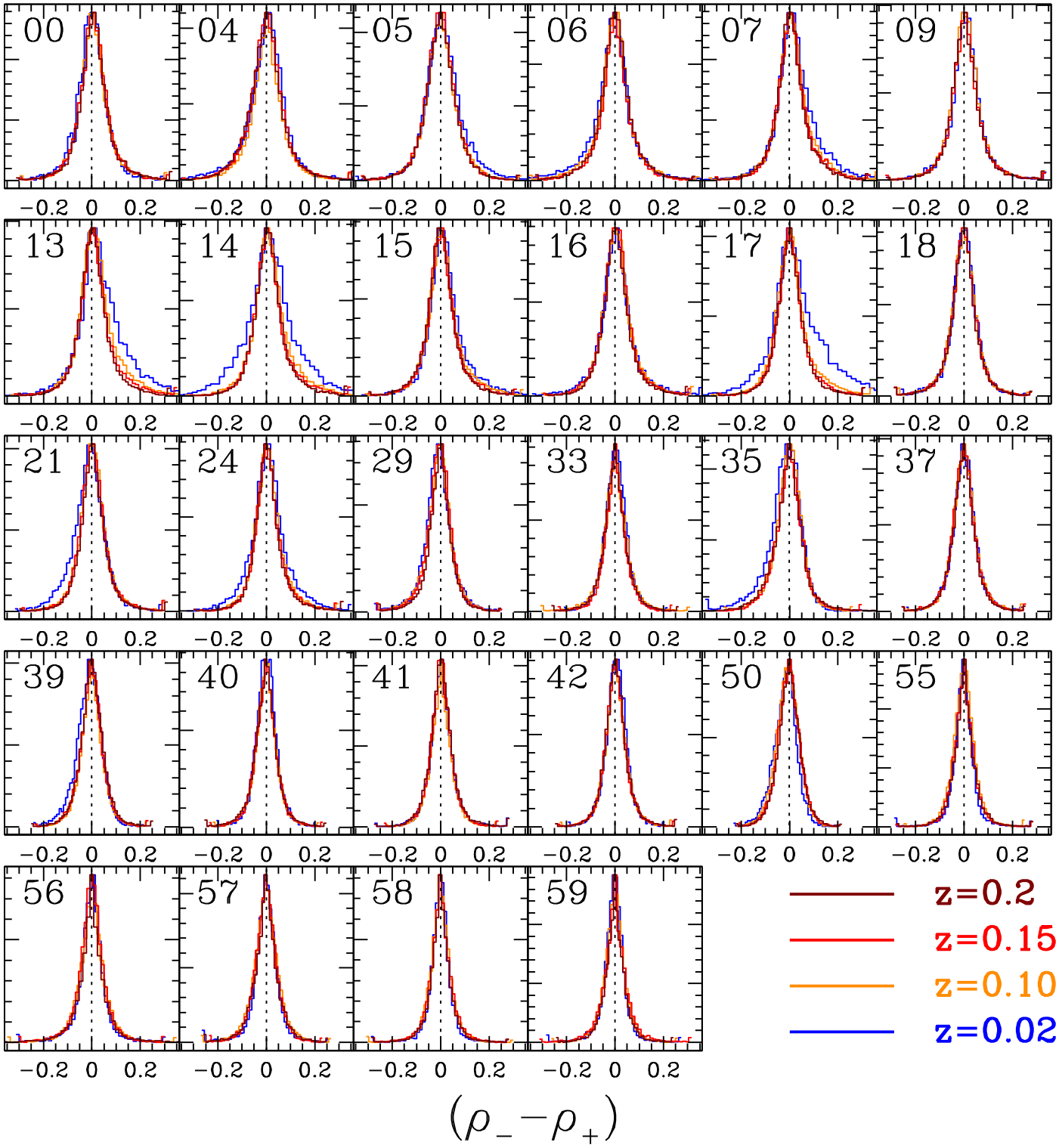

Figure 12. Distribution of the difference between residuals on the blue and the red side of the lines (see Table 1) for several redshift bins. An asymmetric line profile may induce offsets in the derivation of the central position of the line. This figure shows that although some small variations are present in some of the lines, they cannot produce a cumulative effect that would mimic the trend presented in Figure 5.

these residuals as follows:

$$\left.\begin{aligned} \rho_- &\equiv \frac{1}{N_-}\sum_i [\Phi_{\rm OBS}(\lambda_i) - \Phi_{\rm BF}(\lambda_i)]/\sigma_i, \qquad \lambda_i < \lambda_0 \\ \rho_+ &\equiv \frac{1}{N_+}\sum_i [\Phi_{\rm OBS}(\lambda_i) - \Phi_{\rm BF}(\lambda_i)]/\sigma_i, \qquad \lambda_i > \lambda_0 \end{aligned}\right\}, \quad (6)$$

where $\Phi_{\rm OBS}(\lambda)$ and $\Phi_{\rm BF}(\lambda)$ are the observed and best-fit spectra, respectively, and σ_i is the rms uncertainty. The numbers of fitting points on the blue and red sides are N_- and N_+, respectively. A potential skewness would show up as an asymmetry in the distribution of the residuals for a specific line. Figure 12 shows a histogram of the difference, $(\rho_- - \rho_+)$

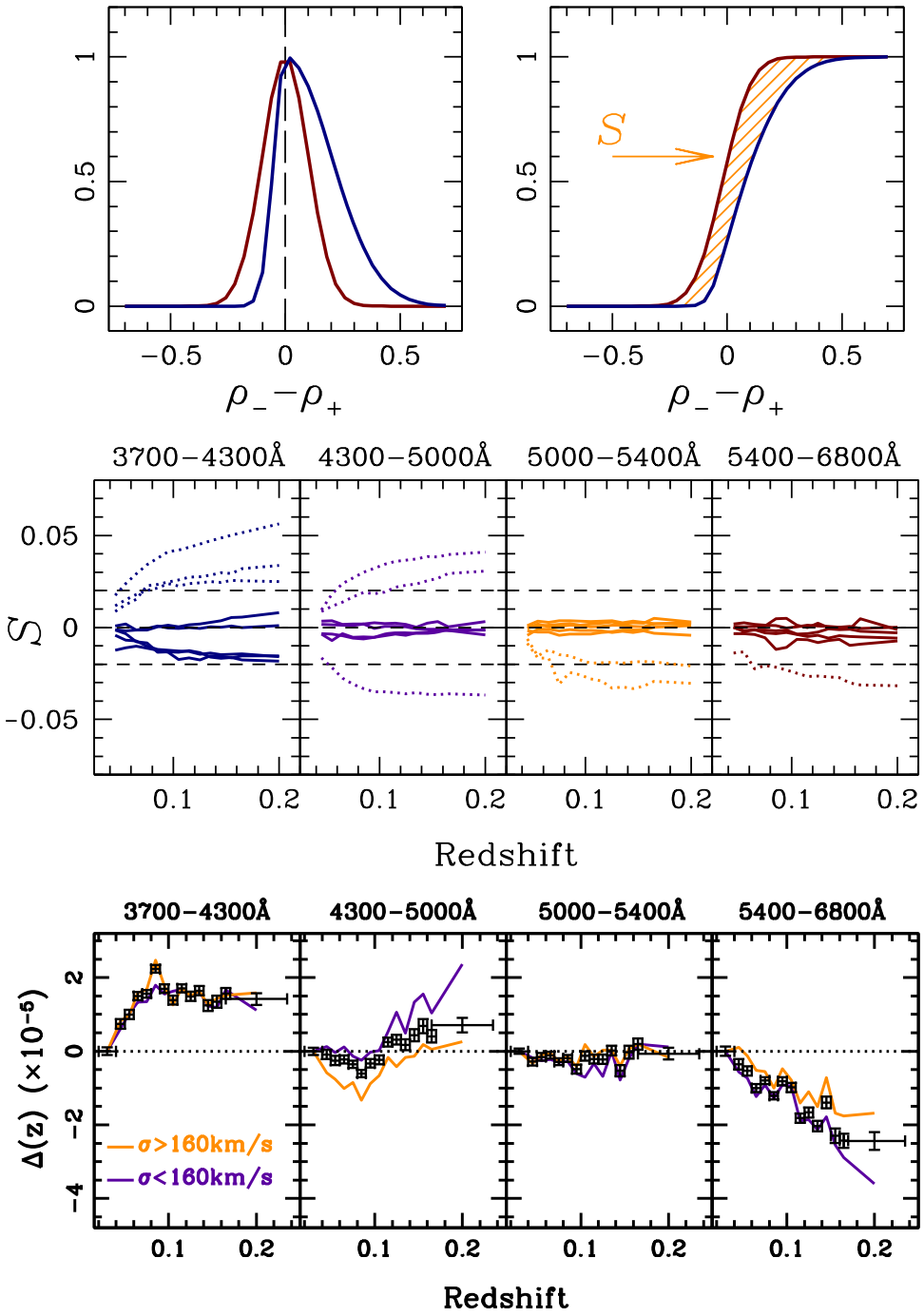

Figure 13. Top: illustration of the quantification of a possible skewness in the line fitting, derived from the difference in the residuals on the blue (ρ_-) and red (ρ_+) sides of the line. The distribution of two typical lines (see Figure 12) is shown in red and blue on the left panel. The difference in area between their cumulative distributions (S, shown in orange, right hand panel) is used as a proxy of the skewness. Note that the comparison is made for the same line in galaxies at different redshifts. Middle: trend of the skewness parameter with redshift. The dotted lines represent the spectral features removed from the analysis, shown in the bottom panel. Bottom: using only the lines with a low value of the skewness parameter S—i.e., rejecting those corresponding to the dotted line in the panel above, we show the redshift and wavelength evolution of $\Delta(z, \lambda_0)$ as in Figure 5. The trend is consistent with our previous findings.

for galaxies in four redshift bins. Note that although small variations among the distributions are apparent, there is no significant trend that could give rise to a cumulative $\Delta(z, \lambda)$, as the one presented in Figure 5. In order to quantify in more detail this result, we define a statistic (S) to measure the skewness. The cartoon in the top panels of Figure 13 illustrates the definition of S for a generic comparison: the histograms of $(\rho_- - \rho_+)$ (left) are shown for two sets—corresponding to the same line in samples at different redshift. Let us assume that the red line corresponds to the distribution at the reference redshift, whereas the blue line is the distribution in a bin at a different redshift. In this example, we assume that one of the sets (the one shown in blue) has a significant skewness. We define our skewness-related statistic S as the area between the cumulative

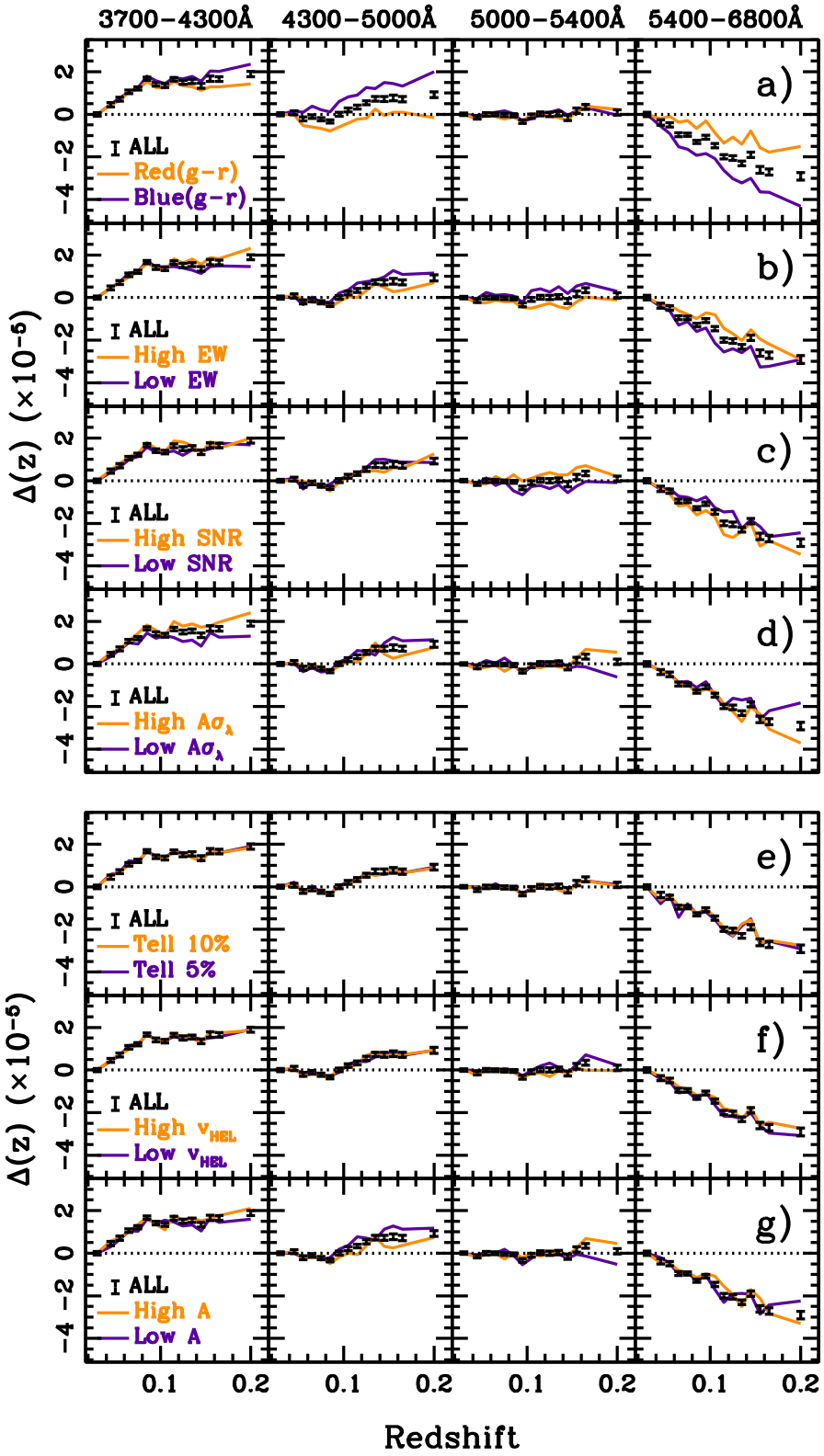

Figure 14. Comparison of $\Delta(z, \lambda_0)$ for different subsamples of galaxy spectra. The observed departures from the standard $(1 + z)$ cosmological law are shown here ($\Delta(z, \lambda_0)$, as defined in Equation (1)). The total sample is shown as error bars (labeled ALL, and being identical to the sample shown in Figure 5). The different rows show the results when splitting the sample at the median value of (a) (g–r) SDSS-fiber color; (b) equivalent width for each of the measured spectral features; (c) signal-to-noise ratio; (d) total area of the Gaussian fit to the features; (e) after rejecting lines affected by a telluric correction above 5% or 10%, as labeled; (f) heliocentric velocity correction applied to the spectra; (g) amplitude of the Gaussian fit. The results consistently show for all cases an offset from the standard $(1 + z)$ law. For ease of comparison, the vertical axis in all the panels extend over the same interval as in Figure 5.

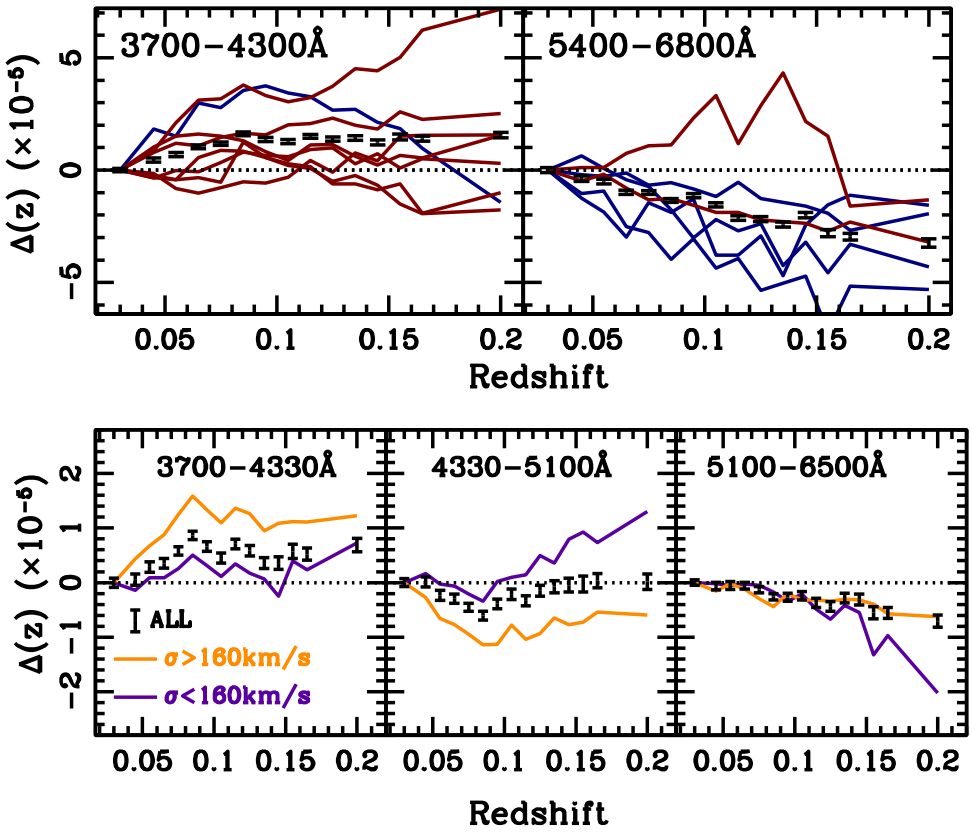

Figure 15. Top: departure from the standard $(1 + z)$ law for individual spectral lines. We show here the trend of $\Delta(z; \lambda_0)$ vs. redshift for the complete sample (error bars), along with the result for the fits for individual spectral features within the rest-frame spectral window given in each panel. Each line is color coded depending on whether the feature is mostly in emission (blue) or absorption (red). Bottom: trend of $\Delta(z)$ with redshift, when all the emission lines are removed from the analysis. Note that we now split the reduced spectral range into three parts.

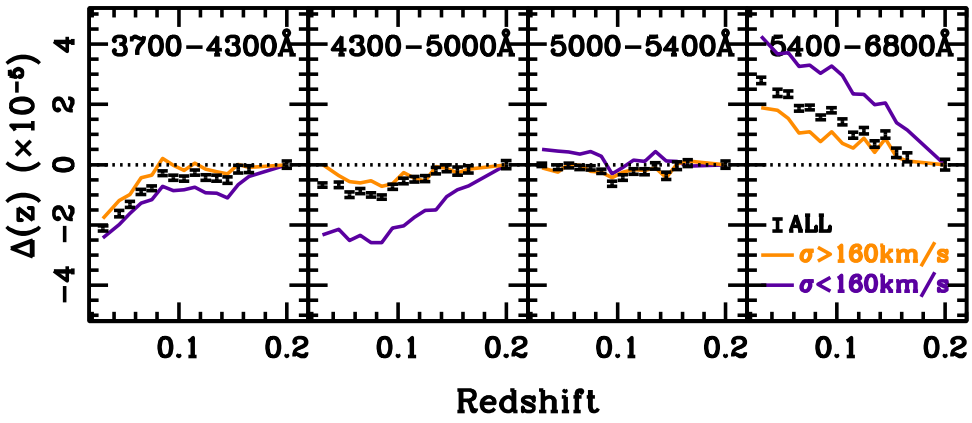

Figure 16. Trend of $\Delta(z)$ with redshift as in Figure 5, with the reference redshift changed to the highest redshift bin ($z = 0.18$–0.25).

distributions (right). Note that this definition preserves the sign: the area between the cumulative distribution of the targeted bin with respect to the reference bin is considered positive/negative depending on whether it lies above/below the reference. In addition, if the difference between the two sets is symmetric about the center (as would be the case for two Gaussians with different widths, or a Gaussian and a Lorentzian), the cumulative distributions will not match, but the total area, S, will cancel out. This method is applied to quantify the *relative* difference in the line profiles for the same line, as a function of redshift. Only if this parameter correlates strongly with redshift *and* wavelength, we can expect a systematic from line shape variations to affect our results. The middle panels of Figure 13 show the behavior of the lines studied in this paper, binned in wavelength in the same way as the result presented in Figure 5. Note that the trend is mild, except for a few cases (dotted lines). In order to test whether this trend could be responsible for the signal reported in this paper, we repeated the analysis, rejecting those lines where $|S| \gtrsim 0.02$. The bottom panel of Figure 13 is the outcome, showing that the trend found in the SDSS spectra is resilient with respect to a skewness-related systematic. Therefore, we

conclude that a simple measure of the asymmetry of the line profiles cannot account for the observed variation.

A.3. Additional Systematics

In order to further test the robustness of the signal measuring the departure of the observed wavelengths with respect to a standard $(1 + z)$ cosmological law, we show in Figure 14 the equivalent of Figure 5 for a different set of subsamples. All panels show the result from the complete sample—selected in velocity dispersion in the range 100–250 km s^{-1}—as error bars, labeled "ALL." Row (a) shows the trend of $\Delta(z, \lambda_0)$ when splitting the sample with respect to the SDSS-fiber color (g–r), after accounting for foreground Milky Way dust attenuation. For each set of measurements within a redshift bin, we split the sample at the median value of the distribution of (g–r). Note that this separation creates a similar result as with respect to the velocity dispersion (Figure 5) or age/metallicity of the stellar populations (Figure 6 and Section 4.1). However the general trend is not removed. The next two rows follow the same procedure, splitting the sample with respect to the equivalent width (b), and S/N (c). In (d) we consider the actual area of the Gaussian fit ($\propto \mathcal{A}\sigma_\lambda$, see Equation (2)). Row (e) explores the contribution from telluric absorption. Here, we reject those measurements where the core of the line—defined as $\lambda_0 \pm \sigma_\lambda$, where λ_0 is the central wavelength of the feature and σ_λ is the width of the Gaussian fit—is affected by a telluric correction above 5% or 10%, as labeled. To estimate the level of correction, we use the atlas of telluric features (from R. W. Hanuschik 2006, private communication) and create a smoothed correction model at the spectral resolution of the SDSS spectrograph ($R \sim 2000$). Row (f) splits the sample with respect to the heliocentric velocity correction applied to the spectra. Finally, we show in (g) the difference with respect to the amplitude of the Gaussian fit ($\mathcal{A}$ in Equation (2)). Note that in all cases the trend presented in Figure 5 is reproduced.

Figure 15 (top) shows a similar plot, where each line represents the trend estimated for a single spectral feature. The lines are color-coded, with blue lines representing features mostly in emission, and red lines corresponding to absorption features. For reference, the error bars show the results presented in Figure 5, which represent the median extended to all measurements from all galaxies and all lines within the rest-frame spectral window given in each panel. Note that aside from the large scatter expected from individual lines, there is a clear trend between the blue- (left) and the red-end (right) of the spectral window. We point out that the information in the blue end is dominated by absorption lines (except for [O II]), whereas at the red end, the situation is reversed, and the emission lines from Hα, [N II], [S II] contribute the most to this wavelength bin. In order to assess whether the observed departure from the $(1 + z)$ law is related to the difference between absorption and emission (i.e., tracing the difference between the gas and the stellar component of the galaxies), we show in the bottom panel of Figure 15 the same analysis as in Figure 5, restricted only to absorption lines. Although on this occasion we need to split the spectral range in three bins, given the reduced set of lines, the result is nevertheless robust against this issue.

Finally, Figure 16 shows the same analysis, when changing the reference redshift—which is needed to define the position of the spectral features—from $z = 0.02$–0.04 (used throughout this work) to the highest redshifts, $z = 0.18$–0.25. Such a change does not affect the result either, except for the expected change in the sign of $\Delta(z)$.

REFERENCES

Abazajian, K., Adelman-McCarthy, J. K., Agüeros, M. A., et al. 2003, AJ, 126, 2081
Abazajian, K. N., Adelman-McCarthy, J. K., Agüeros, M. A., et al. 2009, ApJS, 182, 543
Abdo, A. A., Ackermann, M., Ajello, M., et al. 2009, Natur, 462, 331
Ahn, C. P., Alexandroff, R., Allende Prieto, C., et al. 2014, ApJS, 211, 17
Aihara, H., Allende Prieto, C., An, D., et al. 2011, ApJS, 193, 29
Albareti, F. D., Comparat, J., Gutiérrez, C. M., et al. 2015, arXiv:1501.00560
Amelino-Camelia, G., Ellis, J., Mavromatos, N. E., Nanopoulos, D. V., & Sarkar, S. 1998, Natur, 395, 525
Arai, S., Nitta, D., & Tashiro, H. 2016, arXiv:1605.5852
Arp, H. 1987, Quasars, Redshifts, and Controversies (Berkeley, CA: Interstellar Media)
Balogh, M. L., Morris, S. L., Yee, H. K. C., Carlberg, R. G., & Ellingson, E. 1999, ApJ, 527, 54
Bernardi, M., Sheth, R. K., Nichol, R. C., Schneider, D. P., & Brinkmann, J. 2005, AJ, 129, 61
Brinchmann, J., Charlot, S., White, S. D. M., et al. 2004, MNRAS, 351, 1151
Ciddor, P. E. 1996, ApOpt, 35, 1566
Edlen, B. 1953, JOSA, 43, 339
Fixsen, D. J. 2009, ApJ, 707, 916
Hawkins, K., Jofré, P., Gilmore, G., & Masseron, T. 2014, MNRAS, 445, 2575
Hubble, E., & Humason, M. L. 1931, ApJ, 74, 43
Kroupa, P. 2001, MNRAS, 322, 231
Laio, A., Rizzi, G., & Tartaglia, A. 1997, PhRvE, 55, 7457
Morton, D. C. 1991, ApJS, 77, 119
Oesch, P. A., van Dokkum, P. G., Illingworth, G. D., et al. 2015, ApJL, 804, L30
Press, W. H., Teukolsky, S. A., Vetterling, W. T., & Flannery, B. P. 2002, Numerical Recipes in C++: The Art of Scientific Computing (Cambridge: Cambridge Univ. Press)
Quast, R., Reimers, D., & Levshakov, S. A. 2004, A&A, 415, L7
Rahmani, H., Maheshwari, N., & Srianand, R. 2014, MNRAS, 439, L70
Rogers, B., Ferreras, I., Peletier, R., & Silk, J. 2010, MNRAS, 402, 447
Smee, S. A., Gunn, J. E., Uomoto, A., et al. 2013, AJ, 146, 32
Thomas, D., Maraston, C., & Bender, R. 2003, MNRAS, 339, 897
Trager, S. C., Worthey, G., Faber, S. M., Burstein, D., & González, J. J. 1998, ApJS, 116, 1
Vazdekis, A., Ricciardelli, E., Cenarro, A. J., et al. 2012, MNRAS, 424, 157
Webb, J. K., Murphy, M. T., Flambaum, V. V., et al. 2001, PhRvL, 87, 091301
Wolf, E. 1987, Natur, 326, 363
York, D. G., Adelman, J., Anderson, J. E. Jr, et al. 2000, AJ, 120, 1579